DOE/ET-53088-207 IFSR #207

THREE DIMENSIONAL TOROIDAL MAGNETOHYDRODYNAMIC PARTICLE CODE

F. Brunel, J.N. Leboeuf, D.P. Stotler,*
H.L. Berk, and S.M. Mahajan
Institute for Fusion Studies
The University of Texas at Austin
Austin, Texas 78712

* Division of Physics, National Research Council,
Ottawa, Canada K1A0R6

September 1985

THREE-DIMENSIONAL TOROIDAL MAGNETOHYDRODYNAMIC PARTICLE CODE†

F. Brunel, J.N. Leboeuf, D.P. Stotler*
H.L. Berk, and S.M. Mahajan
Institute for Fusion Studies
The University of Texas at Austin
Austin, Texas 78712

Abstract

The magnetohydrodynamic particle code has been developed to three dimensions in a cylindrical coordinate system in order to describe the plasma in a torus. To keep the noise level down, the finite differences are defined halfway between grid points and the magnetic force is defined in a non-conservative manner, i.e., $\vec{F}_M = (1/4\pi)(\vec{\nabla}\times\vec{B})\times\vec{B}$. Two practical examples of using such a code for physics applications are reported: simulations of high amplitude Global Alfvén Eigenmodes and stabilization of flute modes by a hot electron ring.

† To appear in "Algorithms, Architectures and the Future of Scientific Computation", edited by T. Tajima and F.A. Matsen, The University of Texas Press.

* Permanent address: Division of Physics, National Research Council, Ottawa, Canada K1AOR6.

I. Introduction

The magnetohydrodynamic (MHD) particle codes, which use a particle method to follow the plasma motion on the MHD time scale, have already been extensively developed in earlier works.[1,2] In these codes, the particles represent elements of a fluid in a Lagrangian fashion and their orbits are solved using the MHD force. In return, the fluid moments, such as the mass density and fluid velocities, can be evaluated on a grid by using the particle velocities, in order to advance the magnetic field in an Eulerian way.

In this article, we report on the extension of such codes to the full 3 dimensions and also the extension to the cylindrical coordinate system in order to describe a plasma in a torus. We also report on the required improvement of the numerical techniques.

The main advantage of such a code is that the continuity equation is automatically satisfied and we do not have to solve any of the fluid advective terms since we follow the characteristics of motion. These advantages are clearly seen in the examples given here. Since we do not use any artificial viscosity, we are able to follow the evolution of global Alfvén eigenmodes (which have a very small damping, i.e., $\nu/\omega \simeq 1 - 3\%$) to a very high amplitude level in a diffuse plasma column. Among other improvements, we show in another example how a hot electron plasma can be added to the model in order to describe the stabilization of flute modes due to a hot electron ring in the Elmo Bumpy Torus (EBT).

II. Numerical Highlights

In a cylindrical coordinate system (r, ς, z) described in Fig. 1 with $\varsigma = r_0\theta$, the equations of motion for the fluid particles become

$$\rho\left\{\ddot{r} - \frac{r_0^2\ell^2}{r^3}\right\} = F^r,$$

$$\rho\dot{\ell} = h_\varsigma^2 F^\varsigma, \tag{1}$$

$$\rho\ddot{z} = F^z.$$

The terms F^i (when i denotes the r, ς, or z direction) are the contravariant components of the MHD force $\vec{F} = \vec{F}_p + \vec{F}_M = -\vec{\nabla}p + (4\pi)^{-1}(\vec{\nabla} \times \vec{B}) \times \vec{B}$, while the subscripts pertain to covariant quantities. We use the following metric $d_s^2 = h_r^2\ dr + h_\varsigma^2\ d\varsigma + h_z^2 dz$, where $h_r = h_z = 1$ and $h_\varsigma = r/r_0$. We define an angular momentum $\ell = h_\varsigma^2\dot{\varsigma}$ which allows us to

advance the particles in time using a simple second order accurate (time centered) explicit scheme.

The pressure force term becomes simply $F^i = h_i^{-2}\frac{\partial P}{\partial x^i}$ where $x^i = r, \varsigma$ or z. However, note that the magnetic term can be expressed in many different ways. An ordinary procedure would be to evaluate it in a form that is conservative in a cartesian coordinate system, i.e. $\vec{F}_M = -\vec{\nabla}(B^2/8\pi) + \vec{\nabla}\cdot\vec{B}\vec{B}/4\pi$. But, in the cylindrical coordinate system, this advantage is lost due to the apparition of new terms containing the Christoffel symbols, so that this $\vec{F}_M$ is not conservative any more.[3] If we try to implement F_M in this form, we find an unacceptably high level of noise. A possible explanation is that our code is very sensitive to the type of interpolation used between the grid and particles, in addition to how we define our finite differences.[2] We can exactly satisfy $\vec{\nabla}\cdot\vec{B} = 0$ only in the finite difference sense. However in a cylindrical coordinate system, the second term in $\vec{F}_M$, i.e. $\vec{\nabla}\cdot\vec{B}\vec{B}$ generates a term $\vec{\nabla}\cdot\vec{B}$ which does not vanish exactly anymore in a finite difference sense. This and the addition of new terms due to the presence of Christoffel symbols may generate more errors in the force term, thus enhancing the noise. This problem is not present in cartesian coordinates.

This problem is however circumvented by evaluating the magnetic force as $\vec{F}_M = (4\pi)^{-1}(\vec{\nabla}\times\vec{B})\times\vec{B}$. This becomes in tensoral notation

$$F_M^i = \frac{1}{4\pi h_i^2}\left\{\frac{B_k}{h_k}\frac{\partial}{\partial x^k}(h_i B_i) - \frac{B_k}{h_k}\frac{\partial}{\partial x^i}(h_k B_k)\right\}, \tag{2}$$

where we have a summation over k and the vector components B_i, B_k denote the usual physical components of the magnetic field with i, $k = r, \varsigma$ or z. With this arrangement, we have achieved a noise level as low as in the cartesian system.

We find no numerical problem associated with the magnetic field equation, i.e. $\partial\vec{B}/\partial t = \vec{\nabla}\times(\vec{v}\times\vec{B}) - \eta\vec{\nabla}\times(\vec{\nabla}\times\vec{B})$ expressed in cylindrical coordinates as[3]

$$\frac{\partial B_i}{\partial t} = \frac{1}{h_i h_\ell}\frac{\partial}{\partial x^j}\left\{h_\ell\left(v_i B_j - v_j B_i\right) + \eta\frac{h_\ell}{h_i h_j}\left(\frac{\partial}{\partial x^j}h_i B_i - \frac{\partial}{\partial x^i}h_j B_j\right)\right\}, \tag{3}$$

where we have a summation over j with $j \neq i$ and $\ell \neq i, j$. Equation 3 is advanced as before using the Lax-Wendroff scheme for the advective term (first term on the right) and a first order explicit scheme for the diffusive term (second term on the right.)

In cylindrical coordinates, we find it is also necessary to define all finite differences at a position halfway between grid points as done previously with the pressure term.[2] For

any quantity $A_{i,j,k}$ we then have

$$\left(\frac{\partial}{\partial x^i}A_{ijk}\right)_{i+1/2,j+1/2,k+1/2} = \frac{1}{4}\Big\{A_{i+1,j,k} - A_{i,j,k}$$
$$+ A_{i+1,j+1,k} - A_{i,j+1},k + A_{i+1,j,k+1} - A_{i,j,k+1} + A_{i+1,j+1,k+1} - A_{i,j+1,k+1}\Big\}. \quad (4)$$

Here the main purpose is to improve the accuracy of the derivative in the description of short wavelength modes since the new finite differences span over the grid spacing only instead of 2Δ, as is the case when the differences are evaluated at the grid points themselves.

Since we do not describe the point $r = 0$ (see Fig. 1), it is possible to push the particles in cylindrical coordinates using Eq. 1. The velocities are pushed as follows

$$\dot{r}^* = \left[\dot{r}^{(n-1/2)} + \frac{r_0^2}{r^{(n)^3}}\ell^{(n-1/2)^2} + F_r^{(n)}\right]\Delta t/2,$$
$$\ell^{(n+1/2)} = \ell^{(n-1/2)} + F_\varsigma^{(n)}\Delta t, \quad (5)$$
$$\dot{r}^{(n+1/2)} = \dot{r}^* + \left[\frac{r_0^2}{r^{(n)^3}}\ell^{(n+1/2)^2} + F_r^{(n)}\right]\Delta t/2.$$

Similarly for the positions, with $\ell = (r/r_0)^2\dot{\varsigma}$, we have

$$\varsigma^* = \varsigma^{(n)} + \ell^{(n+1/2)}\frac{r_0^2}{r^{(n)^2}}\frac{\Delta t}{2},$$
$$r^{(n+1)} = r^{(n)} + \dot{r}^{(n+1/2)}\Delta t, \quad (6)$$
$$\varsigma^{(n+1)} = \varsigma^* + \ell^{(n+1/2)}\frac{r_0^2}{r^{(n+1)^2}}\frac{\Delta t}{2},$$

where the superscript n represents the time step, i.e. $t = n\Delta t$. We push the z component with the usual leapfrog method. Equations 5 and 6 represent a simple explicit time-centered numerical scheme which is stable as long as $v\Delta t \lesssim \Delta, r$ which means that the point $r = 0$ must be excluded.

For the boundary conditions, our system is periodic in ς and bounded in r and z with perfect conducting boundaries where the fluid particles are reflected. In the bounded directions guard grid points are used.

III. Nonlinear Global Alfvén Eigenmodes

Global or discrete Alfvén waves (GAE) are a set of the MHD eigenmodes of a current-carrying inhomogeneous confined plasma. Their eigenfrequencies lie below the minimum of $k_{||}(r)V_A(r)$, where r is the direction of inhomogeneity, $k_{||}$ is the wavenumber along the ambient magnetic field $\mathbf{B}_0$, $V_A = B_0/(4\pi\rho)^{1/2}$ the Alfvén speed and ρ the plasma density. These modes are different from the so-called "MHD continuum" which are characterized by $\omega \geq (k_{||}V_A)_{\min}$.

Computer simulations are carried out with our 3D MHD particle code for a square cross-section cylindrical plasma column with its axis along the z-direction.[4] The cylinder is bounded in x and y with perfect conductors and is periodic in z. We use a $16 \times 16 \times 16$ grid. The equilibrium is described by $\vec{B}_0 = \vec{e}_z B_z + \vec{\nabla}\psi \times \vec{e}_z$, with flux function $\psi = (B_{\perp 0}/k)\cos(kx)\cos(ky)$, pressure profile $P(\psi) = \beta k^2\psi^2 + P_0$ and $B_z^2(\psi) = 2(1-\beta)k^2\psi^2 + B_{z0}^2$, with $k = \pi/a$ and $\beta \propto \frac{8\pi P}{B^2}$ can vary freely.

We first run the MHD particle code with a thermal level of fluctuations to study the linear regime. A stable equilibrium is found for $B_{z0} = 3B_{\perp 0}$, $\beta = 0.2$, $L_x = L_y = a$, $L_z = \pi a$ so that on axis $q = 2.07$. In Fig. 2a our profile of q is shown. The density ρ decreases as a function of x making V_A increase towards the boundary. In Fig. 2a we also plot the important quantity $k_{||}V_A = (2\pi/L_z)(\ell + m/q)$ as a function of x for our equilibrium and different values of poloidal mode number m and toroidal mode number ℓ. At each time step the z-transformed magnetic field data ($k_z = 2\pi\ell/L_z$, $\ell = 0, 1, 2, \ldots$) for the full $x-y$ cross-section are stored for $0 < t < T$. An interferogram is obtained by performing the following integral $B_\ell(x, y, \omega) = T^{-1}\int_0^T dt\ B_\ell(x, y, t)\cos(\omega t)$. The frequency is varied over the complete spectrum and for ω corresponding to an eigenfrequency, the eigenmode structure appears in $B_\ell(x, y, \omega)$. The real part of the eigenmode $m = 4$, $\ell = 1$ is displayed in Fig. 2b. The imaginary part is rotated with respect to the real part and from the sense of rotation, we determine that it has the inverse helicity with respect to the magnetic field. The eigenmode is found for $\omega = 1.32 < (k_{||}V_A)_{\min} = 1.43$ from Fig. 2a. The GAE are then spatially nonresonant and have $\omega < (k_{||}V_A)_{\min}$.

To investigate the nonlinear behavior of GAE, an helical antenna is introduced in the plasma cavity at $1 - \frac{1}{2}$ grid point from the wall: the helicity ($m = 4, \ell = 1$) and the pump frequency ($\omega = 1.32$) is chosen to coincide with that of the eigenmode we want to excite. For a strong antenna signal we show in Fig. 3a the plot of magnetic energy versus time for the $m = 4$, $\ell = 1$ antenna. Since the mode is broad and extends to the

outside region, it couples strongly to the antenna. In the linear part of its history, $t \lesssim 56$, the mode behaves like a forced harmonic oscillator. The peak magnetic energy reached at $t = 56$ is very high and corresponds to $\delta B/B_T \sim 10\%$ where B_T is the total magnetic field strength. The saturation mechanism is that of a damped harmonic oscillator. We show in Fig. 3b a plot of the mode energy for $\ell = 0, 1$, and 2. Even though the average magnetic energy in Fig. 3a remains fairly constant after reaching its maximum value, the magnetic energy in the $\ell = 1$ mode (the driven mode) damps away. The energy must go to the other ℓ modes.

Even though the peak magnetic energy reached is very high, we see no evidence of either a strong global MHD or other disruption process. The plasma remains well confined throughout the run and retains its original profile. The plasma equilibrium seems to be able to withstand rather high levels of GAE.

IV. Simulations of the Interchange Instability

The Elmo Bumpy Torus (EBT) device is composed of a series of mirror cells linked into a torus. A hot electron ring resides in each mirror cell. Without the rings, the plasma is unstable against the interchange MHD mode. The diamagnetic well created by the ring can stabilize this instability.

Computer simulations of ring stabilization of the interchange instability are carried out using a $2 - \frac{1}{2}$ version of the particle MHD code.[5] The vertical cross-section of a single mirror cell is considered with a radial gravity as the mirror curvature. The hot electrons characteristic of EBT are modeled by a rigid non-interacting current ring immersed in the main plasma;[6] its effect enters as a $\vec{J}_h \times \vec{B}$ (J_h the ring current, B the total magnetic field) term in the MHD force on the particles. The force on each j-th particle is written as

$$d\vec{v}_j/dt = \rho^{-1}\left(\vec{J}_h \times \vec{B} - \vec{\nabla}P + \rho\vec{g}\right) = \rho^{-1}\left[(\vec{\nabla} \times \vec{B}) \times \vec{B}/4\pi - \vec{\nabla}P + \rho\vec{g} - \vec{J}_h \times \vec{B}\right]$$

since $\vec{J} = (\vec{\nabla} \times \vec{B})/4\pi = \vec{J}_p + \vec{J}_h$.

The following equilibrium is established initially. The pressure profile is chosen to be

$$P(r) = P_0 \begin{cases} 1 & r < r_0 \\ e^{-(r-r_0)^2}/\Delta r^2 & r > r_0 \end{cases}$$

$$P_{\rm hot}(r) = \beta_h \frac{B_0^2}{4\pi} e^{-(r-r_0)^2}/\Delta r^2$$

where $P(r) = \rho^{\gamma}_{\rm ideal}(r)$, β_h is the beta of the ring centered at r_0 with width Δr. The particles are placed so that $\rho_{\rm actual}(x,y) - \rho_{\rm ideal}(r) \simeq 0$. The equilibrium magnetic field is obtained by integration from $\frac{d}{dr}\left(B_z^2/8\pi + P_{\rm actual} + P_{\rm hot}\right) = \rho_{\rm ideal}(r)g(r)$. The current J_h is constant in time and set equal to $\vec{J_h} = B_z^{-1}\frac{d}{dr}P_{\rm hot}\vec{\theta}$. The accuracy of the equilibrium depends on the size of $\rho_{\rm actual} - \rho_{\rm ideal}$ which is minimized with a Gaussian profile and a larger number of particles, typically 64×128 on our 32×32 $x-y$ grid. A representative equilibrium is illustrated in Fig. 4 when the magnetic field $B_z(x,y)$ is plotted in Fig. 4a, the pressure $P_{\rm actual}(x,y)$ in Fig. 4b and the gravity $g(x)$ in Fig. 4c for $\beta_h = 0.9$, $g_0 = 0.03$, and $V_A/c_s = 5.0$.

Typical results are that for $g = 0$ and $\beta_h = 0$, the system is stable as expected. For $g = 0$ and $\beta_h \neq 0$, the plasma is also stable, again as expected. For $g \neq 0$ and $\beta_h = 0$, however, the interchange instability sets in and exponential growth results. The instability is characterized by large vortices at the edge of the pressure gradient. A theoretical analysis of the system with ring yields a growth rate

$$\omega^2 = -g\frac{\left(\frac{d}{dr}\ell n B_0 - \frac{1}{2}\frac{d}{dr}\ell n\ P\right)}{1+\beta_c}\left(1 + \frac{J_h B_0 \beta_c}{\rho g}\right)$$

with $\beta_c = 2P/B_0^2$. Stability is achieved if $\beta_h \lesssim \alpha\frac{\Delta r}{R_c}$, with R_c the radius of curvature and α a constant of order 1. Comparison between theory and simulations is shown in Fig. 5 for the case without ring; the growth rates are both computed and measured at $r = r_0 + 3\Delta r/4$. In the presence of a ring ($\beta_h \neq 0$, and $g \neq 0$), stabilization of the instability is observed for $r \leq r_0 + 3\Delta r/4$ but not for $r \geq r_0 + 5\Delta r/4$. In this case, the instability observed in the simulation is nonlocal while the theoretical stability analysis has been done locally. For $g > 0$ and $\beta_h > 0$, $\omega^2 < 0$ for $r < r_{\rm crit}$ and $\omega^2 > 0$ for $r > r_{\rm crit}$, where $r_{\rm crit}$ is some critical radius. This is the behavior observed in the simulations with $r_{\rm crit} \simeq r_0 + \Delta r$.

In summary, the interchange mode is stabilized by a rigid ring, as expected. The MHD particle code has been used to show this. Extensions of the code to include ring interactions and 3D effects are desirable for future investigations.

V. Summary

The MHD particle code has been extended to three dimensions and toroidal geometry. It has shown its versatility in its applications to nonlinear Global Alfvén Eigenmodes in a plasma column and to the interchange instability in a mirror cell of the Elmo Bumpy

Torus device. This shows that strongly nonuniform plasmas can be successfully simulated with the MHD particle code.

Acknowledgments

We acknowledge the collaboration of Professor T. Tajima during the course of this work. This work was supported by the U.S. Department of Energy contract no. DE-FG05-80ET-53088, and the National Science Foundation grant no. ATM-82-14730.

References

1. J.N. Leboeuf, T. Tajima, and J.M. Dawson, J. Comp. Phys. **31**, 379 (1979).
2. F. Brunel, J.N. Leboeuf, T. Tajima, J.M. Dawson, M. Makino, and T. Kamimura, J. Comp. Phys. **43**, 268 (1981).
3. D. Schnack and J. Killeen, J. Comp. Phys. **35**, 110 (1980).
4. F. Brunel, J.N. Leboeuf, and S.M. Mahajan, Phys. Rev. Lett. **54**, 1252 (1985).
5. D.P. Stotler, F. Brunel, T. Tajima, and H.L. Berk, Bulletin of the American Physical Society **29**, 1416 (1984).
6. D.B. Nelson and C.L. Hedrick, Nucl. Fusion **19**, 238 (1979).

Figure Captions

Fig. 1 Schematic illustration of the geometry.

Fig. 2 Gobal Alfvén Eigenmode: a) q and $k_{||}V_A$ profiles; b) $m = 4$, $\ell = 1$ eigenmode with $\omega = 1.32$.

Fig. 3 Global Alfvén Eigenmodes. Time evolution of: a) the total magnetic field energy and b) the energy in various ℓ modes.

Fig. 4 Interchange instability in EBT: a) Magnetic field, b) pressure and c) gravity profiles.

Fig. 5 Interchange instability in EBT. Comparison of theory (solid curve) and simulations (circles and triangles).

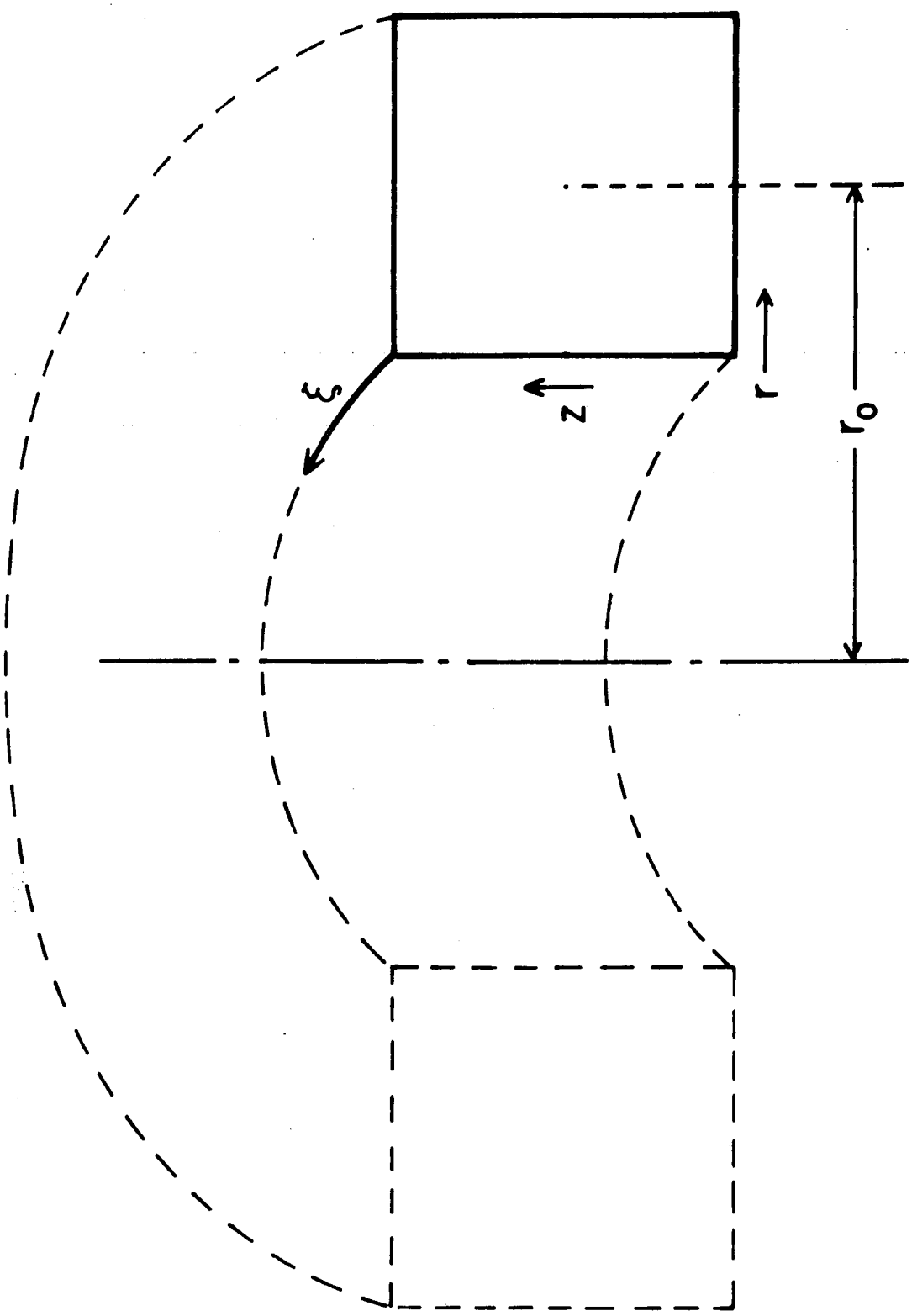

Fig. 1

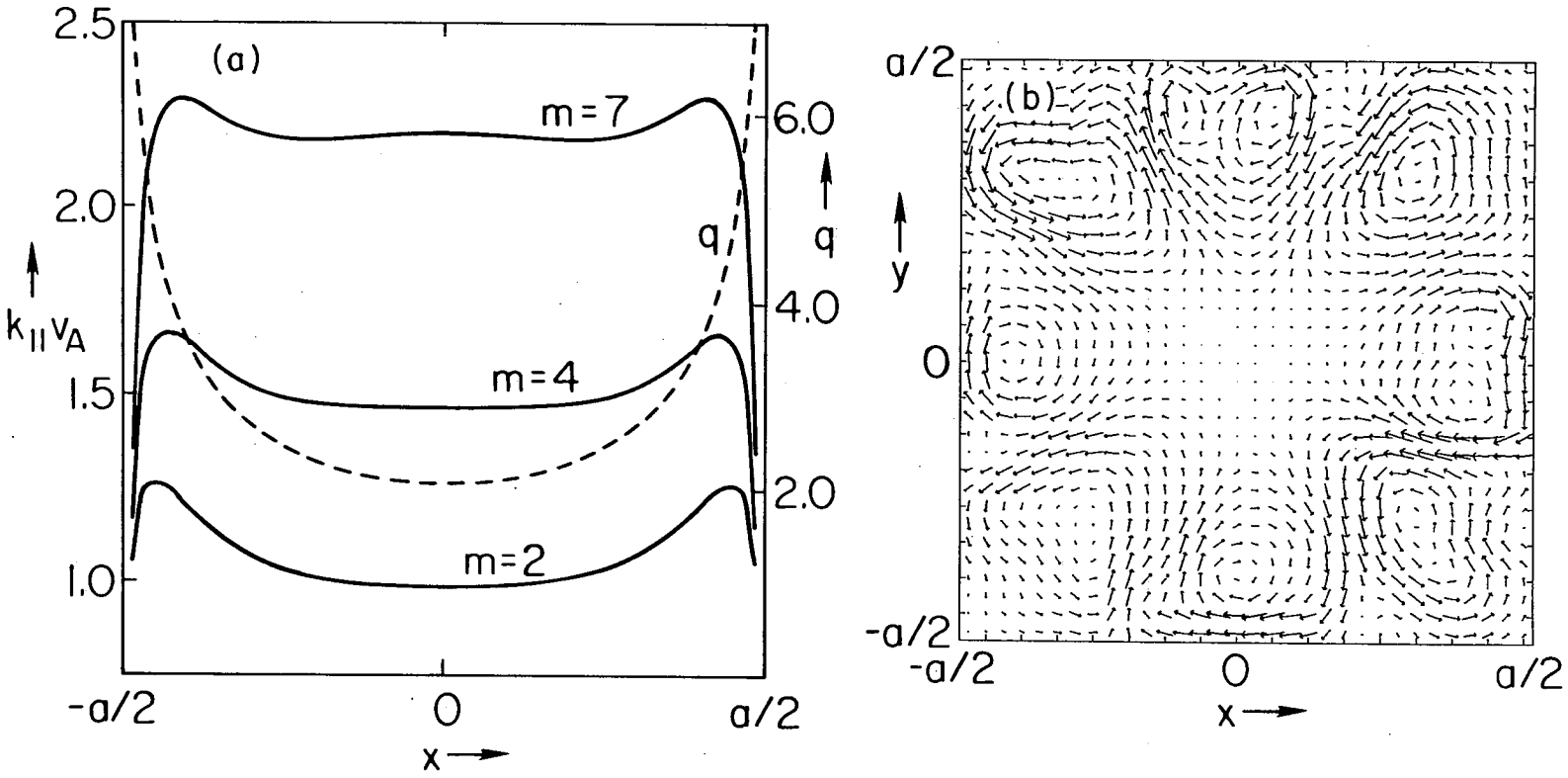

Fig. 2

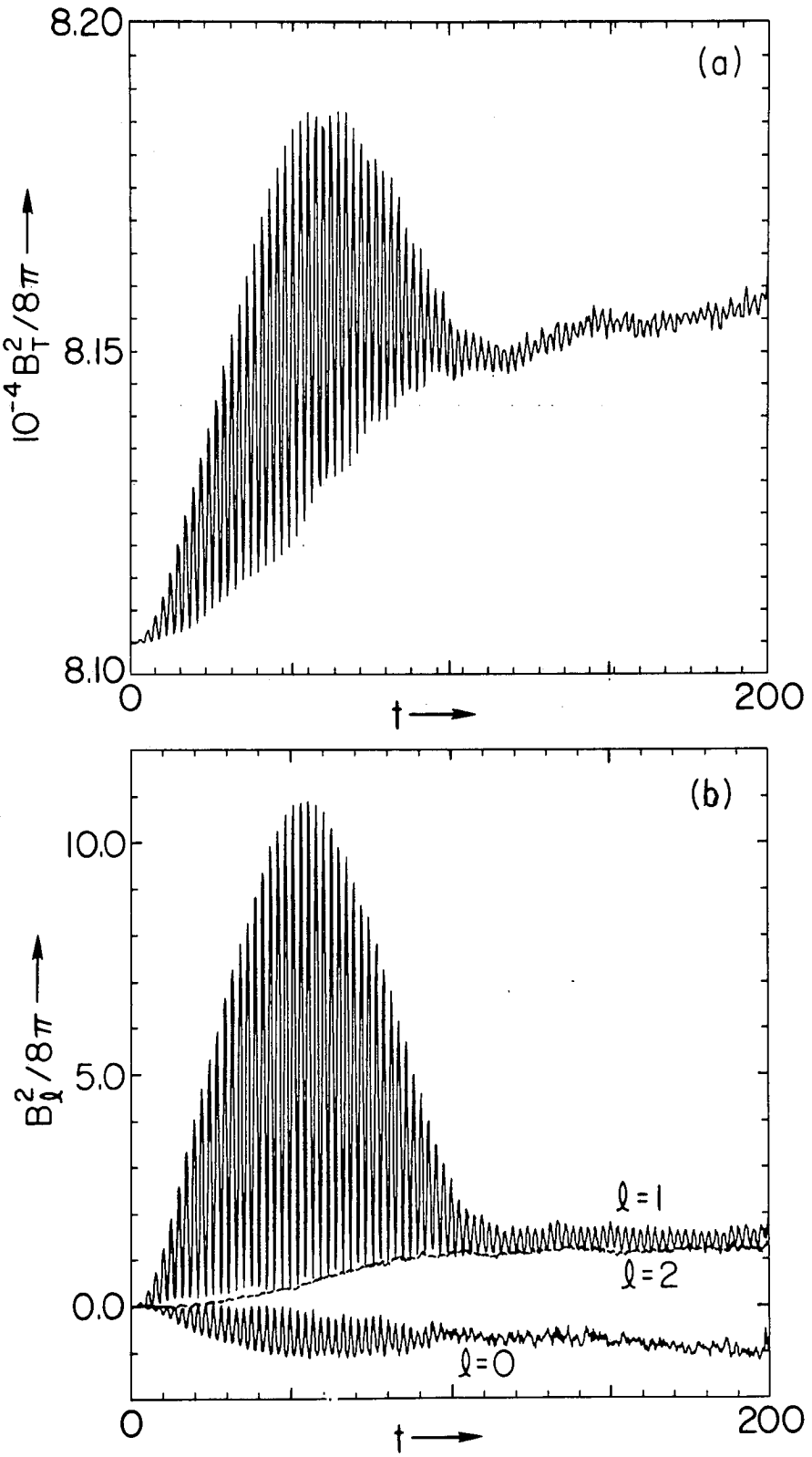
8.20
8.15
8.10
(a)
$10^{-4}B_T^2/8\pi$ ⟶
0
200
t ⟶
(b)
10.0
5.0
0.0
$B_\ell^2/8\pi$ ⟶
ℓ=1
ℓ=2
ℓ=0
0
200
t ⟶

Fig. 3

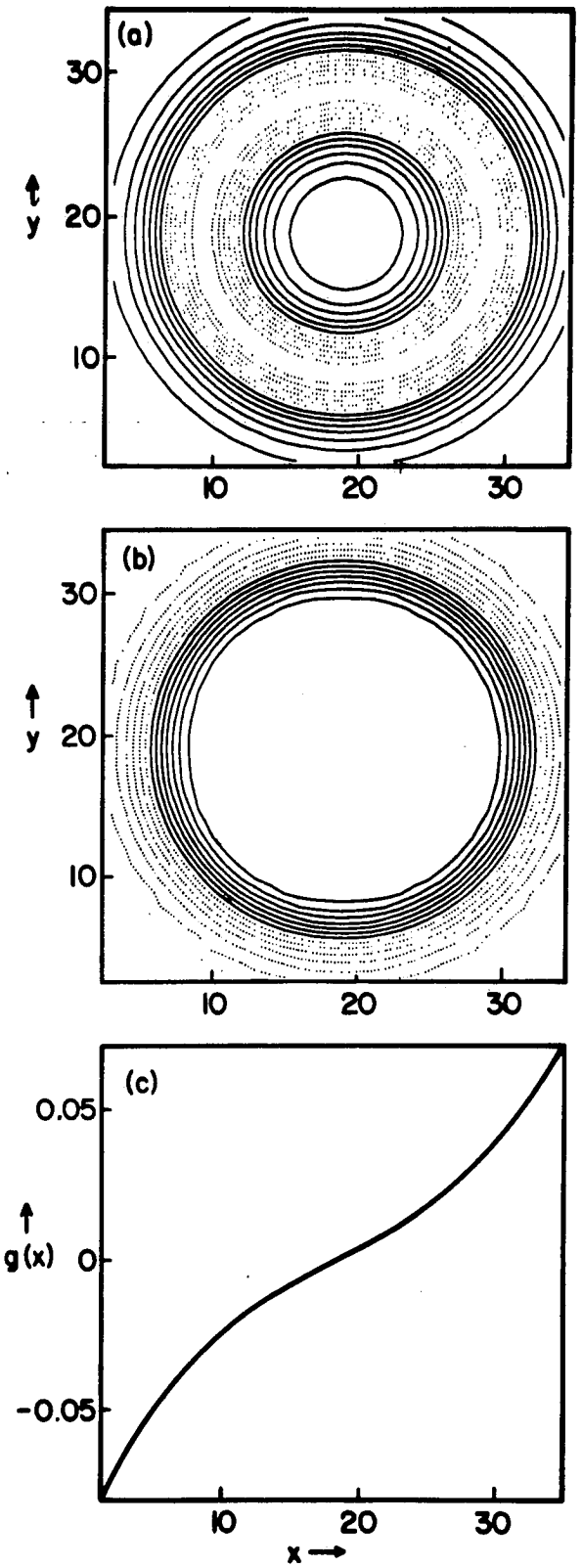

Fig. 4

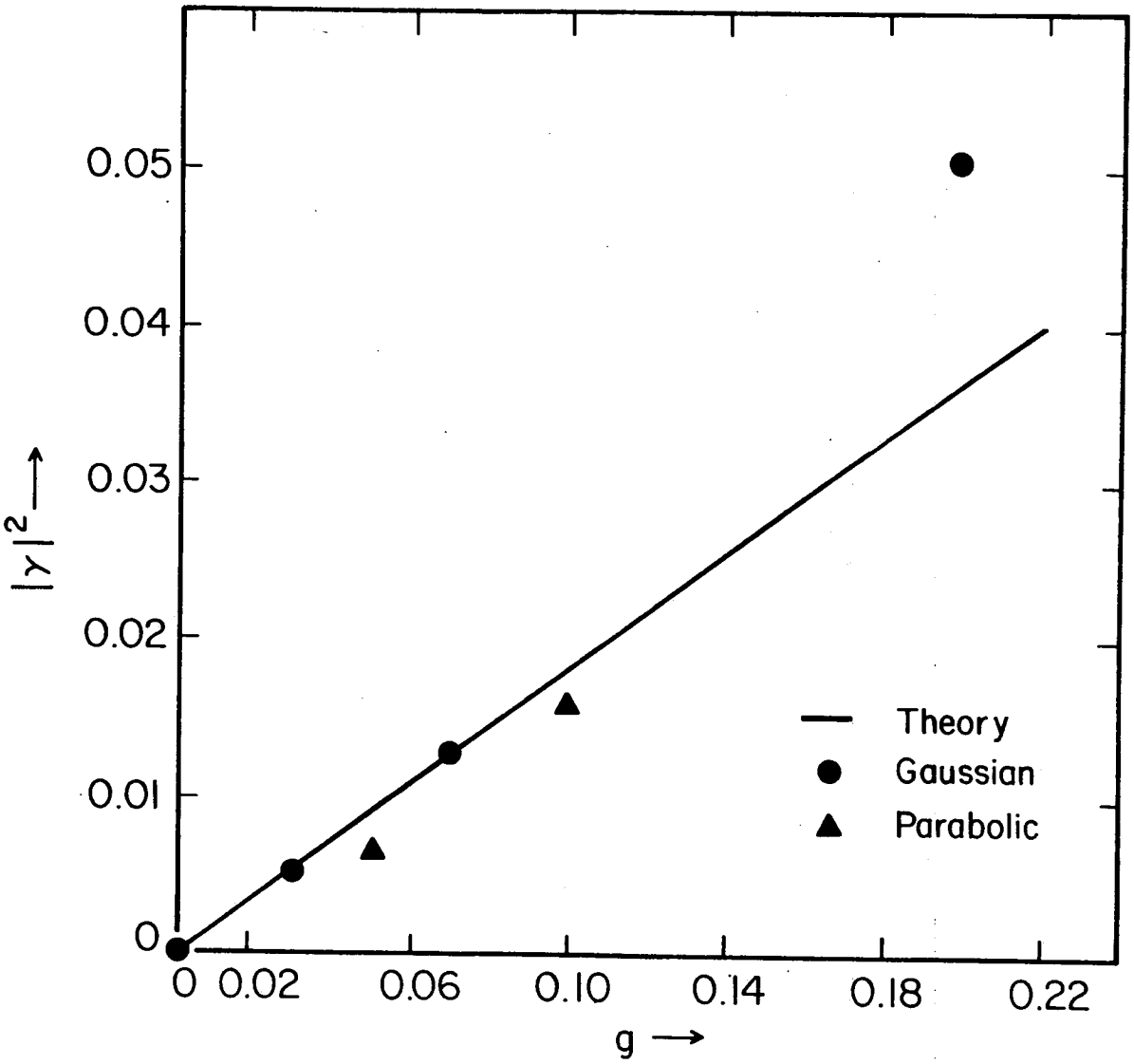
0.05
0.04
0.03
0.02
0.01
0
$|\gamma|^2 \longrightarrow$
0
0.02
0.06
0.10
0.14
0.18
0.22
g ⟶
Theory
Gaussian
Parabolic

Fig. 5